JOINT EUROPEAN TORUS

JET–P(90)39

R. Barnsley, U. Schumacher, E. Kallne, H.W. Morsi, G. Rupprecht
and JET Team

Double Crystal X-Ray Spectroscopy at JET

Double Crystal X-Ray Spectroscopy at JET

R. Barnsley, U. Schumacher[1], E. Kallne[2], H.W. Morsi, G. Rupprecht[3]
and JET Team*

JET-Joint Undertaking, Culham Science Centre, OX14 3DB, Abingdon, UK

[1]Max-Planck-Institut fiir Plasmaphysik, Association EURATOM-IPP, D-8046 Garching, FRG
[2]Department of Physics I, Royal Institute of Technology, S-10044 Stockholm, Sweden
[3]European Southern Observatory (ESO), D-8046 Garching, FRG
** See Appendix 1*

Preprint of Paper to be submitted for publication in
Review of Scientific Instruments

Double-Crystal X-Ray Spectroscopy at JET

R. Barnsley, U. Schumacher[1], E. Källne[2], H.W. Morsi and G. Rupprecht[3]
JET Joint Undertaking, Abingdon, OX14 3EA, UK
[1] Max-Planck-Institut für Plasmaphysik, Association EURATOM-IPP, D-8046 Garching, FRG
[2] Dept. of Physics I, Royal Institute of Technology, S-10044 Stockholm, Sweden
[3] European Southern Observatory (ESO), D-8046 Garching, FRG

A double-crystal monochromator has been brought into operation at JET to measure absolute wavelengths and intensities of impurity spectral lines in the soft X-ray region from about 0.1 nm to 2.3 nm. It is capable of operating also during the deuterium-tritium (active) phase of JET because its detector is very effectively shielded against neutrons and hard X-rays. The spectrometer has been swept over a wide wavelength range, around characteristic line groups as well as monochromatic line scans.

INTRODUCTION

Soft X-ray spectroscopy of magnetically confined high-temperature plasmas provides a range of diagnostic information relating to the concentration, transport and temperature of impurity ions [1–4]. Since high-Z impurities in DD (and DT) plasmas contribute substantially to the plasma power losses and low-Z impurities lead to D (or T) dilution and hence to fusion reaction rate reduction, detailed investigations of the impurity behaviour are a necessary basis for power balance studies. To perform such studies a spectrometer must cover a wide spectral range.

The high temperature DT plasma anticipated in the JET active phase will produce high fluxes of neutrons and γ-rays. This requires good shielding of the detector (reducing the background radiation by about 9 orders of magnitude) and of various components of an active phase crystal spectrometer. Since a wide spectral range must be covered, the need to retain shielding of the beam path over a wide range of Bragg angles places severe constraints on the design of such an instrument.

The scheme of a double-crystal monochromator was chosen because it offers excellent shielding against neutrons and γ-rays due to a labyrinth radiation shield. Since the detector is at fixed angle for all wavelengths[5,6] the shield can be built around it and

the X-ray beam path. Fast wide spectral scans can be performed, and with an appropriate selection of crystals a wide spectral range (0.1 to 2.3 nm) can be covered. The relatively simple optical configuration facilitates absolute calibration for sensitivity and wavelength.

I. THE ACTIVE PHASE DOUBLE-CRYSTAL MONOCHROMATOR

A. The device

The scheme of the shielded double-crystal monochromator is given in Fig. 1. The input and output beams of the soft X-rays from the plasma are fixed for all wavelengths. The plane crystals are positioned by high precision drive mechanisms to fulfil the Bragg condition

$$n\lambda = 2d \cdot sin\Theta \cdot (1 + \frac{4d^2\delta}{n^2\lambda^2}) \tag{1}$$

where λ is the wavelength, 2d the crystal lattice constant, Θ the Bragg angle, n the order of interference and δ is the refractive index minus unity. For any given crystal δ/λ^2 is approximately constant. The positions are controlled by a fast digital servo system[6]. The lattice planes of both crystals have to be parallel within an angular margin much smaller than the double-crystal rocking curve width, in order to maintain constant throughput of the monochromator. This is achieved by the control system to about 6 arcsec in the full Bragg angle range from 26° to 60°.

The resolving power

$$\lambda/\Delta\lambda = (1/\Delta\Theta) \cdot tan\Theta \tag{2}$$

of the instrument can be varied with the angular width $\Delta\Theta$ (FWHM) defined mainly by remotely interchangeable coarse ($1/\Delta\Theta = 1200$) and fine ($1/\Delta\Theta = 10000$) gridded collimators. In order to keep the geometrical orientation of the collimators constant relative to the linear displacement tables all the units of the monochromator are mounted on the same massive epoxy resin concrete plate[6]. The guides for the longitudinal motion, together with the linear (by linear motors) and rotary (by torque motors) drives, are assembled in two rectangular vacuum chamber modules. Each guide rests on three support points, and is adjusted from the outside (atmospheric side) by means of spindles, housed in bellows feedthroughs[6].

At the entrance of the X-ray beam into the monochromator a remotely deployable calibration source is installed which serves two main purposes, namely to align the crystals for parallelism and to obtain an absolute wavelength calibration. The combination of high resolution angle encoders and the fine collimator allows an absolute wavelength calibration and wavelength resolution sufficient for Doppler broadening and line shift measurements.

The detector is a multiwire gas proportional counter (MWPC) with thin polymer window for which the gas pressure, high voltage, and pulse height window can be controlled automatically to suit the observed wavelength range. This gives a high quantum detection efficiency and allows background rejection and selection of the desired diffraction order by pulse height analysis. In order to take advantage of multiple diffraction orders (and thus extend the wavelength coverage of the instrument) the detector signal is fed in parallel to 8 separate single channel analysers which are set to a range of energy windows. Thus the data is stored in 8 memory locations each representing a different energy window, and this coarse multichannel analysis allows identification of the diffraction order of a particular spectral line. Alternatively, the 48 anodes can be connected into 8 groups, each with its own signal processing chain, allowing signal-plus-background count rates of $\sim 10^7 s^{-1}$ without serious pile-up[7].

All instrument and vacuum system functions can be controlled automatically by the JET control and data acquisition system (CODAS).

The double-crystal monochromator in its shielding house is located behind the torus hall wall[6]. The X-rays from JET enter the instrument via a long evacuated beam line through a small penetration in this wall, the JET biological shield, as schematically drawn in Fig. 2.

The design of the double-crystal monochromator shielding is based on the assumption that during deuterium-tritium operation of JET about $6 \cdot 10^{19}$ neutrons of 14 MeV will be emitted per second, resulting in fluxes of neutrons of about $2 \cdot 10^{16} n/(m^2 \cdot s)$ and of gammas of about $7 \cdot 10^{15} \gamma/(m^2 \cdot s)$ near the inside of the torus hall walls. About half of the neutron flux will be isotropic, the other half will be highly directional.

The shielding concept hence consists of a concrete "collar" tightly fitting around the vacuum tube, the narrow beam duct through the wall and two baryte concrete chambers

behind the wall housing the vacuum vessels for the two crystals. This is schematically shown in Fig. 2, where, however, the shielding wall between the two vessels is not drawn (in contrast to Fig. 1).

The shielding outlay is optimized such that each of the possible paths for important radiation transport contributes about the same fraction to the total flux at the detector[5]. There are four main paths for the neutrons, the first by multiple reflections of neutrons (entering through the beam duct) from the first crystal vessel through the connection duct to the second vessel and then to the detector, the second the same, except that the radiation passes through the concrete between the vacuum vessels for the two crystals, the third by penetration of the neutrons through the sides of the duct and the torus hall wall to the second vacuum vessel, and the fourth by neutron streaming from the first vacuum vessel through the shielding to the detector.

Together with the flux of gamma quanta created by neutron interactions in the vicinity of the detector the estimates[5] result in a total neutron plus gamma ray flux of as low as about $10^7(n+\gamma)/(m^2 \cdot s)$. Hence the background radiation can be reduced by about 9 orders of magnitude.

B. Spectral properties and tests of the active phase double crystal monochromator

For the impurity investigations in JET several X-ray spectral regions are of interest, ranging from the wavelengths of the hydrogen- and helium-like transitions of medium-Z impurities (like nickel) to those of low-Z impurities (like oxygen) or neon-like metal lines. Due to the finite monochromator vacuum vessel length the accessible Bragg angle range is limited to between about 26° and 60°. Fig. 3 demonstrates that for this angle range several crystals are suitable to cover the wavelength ranges of most interest, and the observable ionization stages of typical impurities. A similar spectral range is also covered by a spatially scanning double crystal monochromator[8], which is also installed at JET.

It is a necessary condition that the crystal diffraction properties be uniform over the whole crystal surface area. The diffraction properties of most of the crystals were measured over the full crystal surface area[9].

The crystal property tests performed during the preparation phase of the monochromator[9] can be repeated and partly extended with the monochromator itself by using the remotely deployable X-ray calibration source. Using an inconel anode - the same material as for the JET vessel was chosen for simulation of the most prominent metal impurities - the crystal rocking curve widths and the collimator transmission were determined.

Fig. 4 gives an example of the double-crystal rocking curves of Topaz(303) taken at the Kα_1 lines of Ni, Fe and Cr, indicating the increase of the rocking curve width with wavelength. These widths are slightly larger than those found previously[9], because the angular width in non-dispersive direction for these calibration tests was not negligible and since a relatively large crystal area was illuminated contributions from regions of the crystals with slightly different orientation broadened the rocking curves. These measured rocking curve widths are small enough for high resolution spectroscopy if combined with a low acceptance angle collimator. The rocking curve widths of TlAP are wider as can be seen from the example in Fig. 5, taken at NiL$\alpha_{1,2}$ (1.4595 nm), in good agreement with M. Lewis' data[10].

In addition to the previous collimator tests[11,12], the collimator angular transmission was also measured in situ with the monochromator and the X-ray calibration source by parallel rotation of the two crystals. An example is given in Fig. 6, showing the CrKα spectrum taken with Topaz(303) crystals and the fine collimator. The components CrKα_1 and CrKα_2 are well separated, their intensity ratio is in the range of 2, and the line widths appear by 20 to 30 % wider than the natural line width due to the folding with the 41 arcsec (21 arcsec FWHM) wide collimator acceptance angle and the rocking curve width. This result is consistent with the instrumental resolving power $\lambda/\Delta\lambda = (1/\Delta\Theta) \cdot tan\Theta$ of about 9000 at these wavelengths around 0.23 nm, dropping monotonically to about 5000 at 0.16 nm. These values are sufficient to perform line profile measurements, for instance to determine ion temperatures from Doppler broadening.

The tests of the position control of the crystals were carefully performed since the parallelism of both crystals at every instant during the measurements is the most important condition to be fulfilled for the double-crystal monochromator. The angles are read by rotary encoders and the incremental signals from the encoders are fed into a fast

digital feedback system, which controls the angular motions with a time cycle of 3 ms. The rotation angles are determined by incremental encoders which have electrooptical transducers and use amplitude and phase resolution to achieve an accuracy of 2.25 arcsec.

The incremental encoder signals are stored in memory together with the detector signals, allowing the crystal positions to be correlated with the count-rate throughout the discharge. This gives an absolute wavelength scale from within the stored data and allows a check to be made on the parallelism between the two crystals.

An example of the angle difference of both crystals from these encoder readings taken from a typical wavelength scan during a JET discharge is given in Fig. 7. The top trace shows the parallelism of the two crystals during the discharge measured using the two encoders (which are also separately displayed). The result shows that the two crystals stay parallel within 6 arcsec which means that crystals with such narrow rocking curve could be used in the instrument.

Absolute intensity measurements can be performed with the double crystal monochromator after its calibration with the large-area X-ray source[13] developed specifically for absolute calibrations and tests of this instrument and the spatially scanning double-crystal monochromator[8]. The calibration was done by scanning through the wavelength region of the K_α lines of the large-area X-ray source, which was installed in front of the monochromator, in an identical procedure as scanning through the wavelength region of the spectral lines from the JET plasma, both crystals always being kept parallel to each other. If the crystals are rotated at an angular velocity $\omega[rads^{-1}]$ the solid angle integrated spectral line intensity $I_s[photons \cdot m^{-2} \cdot s^{-1}]$ results in a detector count number N. Hence the calibration factor C relating I_s and ω to N by $N = CI_s/\omega$ can be determined. Values of C from calibrations at NiKα and CrKα applying nickel and chromium anode plates, respectively, are plotted in Fig. 8 as open circles.

Additionally, the calibration factor C can be estimated from the crystal properties (as partly determined separately[9]), the geometrical conditions and the detector efficiency. If both crystals are always kept parallel to each other and if we assume that vertical divergence, misalignment, and tilts are all negligible, the number of counts N measured with the detector for a wavelength scan across the line is proportional to the total

line intensity $I_L = \int I_\lambda d\lambda [photons \cdot m^{-2} s^{-1} sr^{-1}]$, to the projected crystal area F_c, the acceptance angle χ perpendicular to the plane of dispersion, the collimator acceptance angle $\Delta\Theta$, the wavelength dependent transmission η_λ (e.g. window absorption, detector efficiency), the structural transmission η_s (e.g. from grids and meshes) and to the integral over the sum of the squares of the polarization components of the single crystal response function [14] $1/2 \int \sum_p (C_n^p(v))^2 dv$, where n is the reflecting order and p denotes the polarization. Note that N is again inversely proportional to the angular velocity ω of the rotating crystals.

$$N = \frac{I_L \cdot F_c \cdot \chi \Delta\Theta \cdot \eta_\lambda \eta_s}{\omega} \int \sum_p (C_n^p(v))^2 dv \tag{3}$$

As a result the calibration factor

$$C = \frac{N\omega}{I_s} = \frac{N\omega}{4\pi I_L} = F_c \cdot \frac{\chi \cdot \Delta\Theta}{8\pi} \cdot \eta_\lambda \eta_s \int \sum_p (C_n^p(v))^2 dv.$$

can be calculated from the separately determined quantities. In separate measurements it was found for Topaz(303), that $1/2 \int \sum_p (C_n^p(v))^2 dv$ can be approximated by the product of the previously determined double crystal integrated and peak reflectivity[9]. Hence for Topaz(303) crystals the values for C are additionally plotted versus the wavelength λ as solid line in Fig. 8.

II. FIRST RESULTS OF X-RAY LINE EMISSION FROM JET MEASURED WITH THE ACTIVE PHASE DOUBLE-CRYSTAL MONOCHROMATOR

The double-crystal monochromator can be operated in different modes (scanning or non-scanning) that give significantly different information on the plasma source. The operational modes are described as:
Covering the Bragg angle range from about 26° to 60° broad band spectra can be taken in a time of down to about one second. By using crystals such as Topaz(303), LiF(220), Gypsum, TlAP and KAP the wavelength range from about 0.12 nm to about 2.3 nm can be covered.

Repetitive scans of a smaller wavelength interval can be taken to study the time evolution of a certain group of spectral lines.

A line scan mode records the profile of a certain spectral line many times throughout the discharge in order to follow the time behaviour of the line width and its intensity. In this mode the translation stages are held by brakes.

The fourth operational (monochromatic) mode is the time behaviour of a spectral line measured with high time resolution.

A. Broad band spectra

Spectra over a wide spectral range are normally taken during a time interval in which the plasma parameters might change. Hence these changes have to be taken into account for the spectral evaluation. An example of a broad-band spectrum taken with TlAP crystals is given in Fig. 9, showing some Ne-like Ni lines and some members of the oxygen Lyman series. The data shown is not corrected for instrument sensitivity calibration. These spectra immediately give an overview of the presence of impurity ions in the JET plasma as well as on their relative abundance.

Broad band spectra in the short wavelength range taken with Topaz(303) or with LiF(220) crystals mainly showed the He-like transitions of Ni and Cr, while those recorded with Gypsum crystals predominantly gave Li-, Be-, B- and Ne-like lines of Ni. However, the Gypsum crystals, although protected by a thin Al coating and vacuum-sealed to avoid evaporation, showed strong reflectivity degradation in vacuum even after a few hours.

These broad band spectra allow absolute wavelength calibration and absolute line intensity measurements after calibration with the large-area X-ray source.

B. Repetitive scans of spectral line groups

The time evolution of characteristic line groups of the He-like transitions of Ni, Cr and Cl can easily be investigated by repetitive scans. An example of the time behaviour of Ni XXVII is given in Fig. 10, taken with the coarse collimator and hence, with relatively low spectral resolution. In Fig. 11 these He-like spectra are plotted versus wavelength λ for Cl, Cr and Ni. The chlorine spectrum was obtained with fifth order reflection from KAP crystals, while the Cr and Ni spectra were taken with Topaz(303) crystals in first order. The intensity ratios of the different lines and the line profile allow electron and ion temperature determination, respectively[1,15–18]. For example, for spectra of He-like

nickel recorded with the fine collimator the Doppler width was measured, allowing ion temperatures typical of JET (3 to 12 keV) to be derived within an error of 15 %.

Another example for repetitive scans of line groups is that of the oxygen Lyman series given in Fig. 12. This scan was taken with TlAP crystals and using the coarse collimator. (The coarse collimator was used to achieve a high signal-to-noise ratio.) It covers the spectral range from 1.37 nm to 1.65 nm and thus contains up to six oxygen Lyman lines (except Lyα), fluorine Lyα (at 1.4984 nm) and some contributions from metal lines below the oxygen Lyman series limit at 1.4223 nm. The limited number of oxygen Lyman lines to be observed is given by the finite resolving power of R = $\lambda/\Delta\lambda \simeq 540$ due to the TlAP rocking curve width of 220 arcsec (see Fig. 5) and the collimator acceptance angle of about 165 arcsec (FWHM). The maximum quantum number n_{max} observed here is 8. This can be roughly confirmed by calculation using the equality of the apparatus profile width $\Delta\lambda_{App} = \lambda/R$ and the wavelength difference $\Delta\lambda = 2\lambda/n^3_{max}$ of the two neighbouring lines (Doppler and Stark profile contributions are negligible for these plasma parameters) resulting in $n_{max} \simeq (2R)^{1/3} \approx 10$.

Since generally hydrogen-like spectra are theoretically well understood, the intensities of the Lyman lines (applying eq. (3)) versus the quantum number n normalized to the Lyman-α intensity are shown plotted in Fig. 13. The intensity distribution is compatible with the dependence as to be expected from collisional excitation[19]. One potential of this data analysis would be to identify influence of charge exchange excitation, since this would increase the intensity ratio for certain quantum numbers.[20]. Since the calculations do not take the level population by charge exchange processes into account it is suspected that these might be responsible for the higher intensities in the higher n members.

C. Line scans

A scan of the profile of a certain spectral line can be performed many times throughout the discharge in order to follow the time behaviour of the line width and the line intensity. Fig. 14 gives an example of such a line scan for Ni XIX and O VIII for two similar plasma discharges at JET. The variations of line intensities, measured with high temporal resolution, e.g. 10 profiles per second in Fig. 14, show clearly that the sensitivity of the monochromator is high enough to reveal the different behaviour of oxygen and nickel during x-point operation and neutral beam injection[21].

For detailed line profile measurements with the aim to measure ion temperature and toroidal rotation the high resolution collimator is used ($\lambda/\Delta\lambda$ = 10 000). Using a pair of Ge(111) crystals the total instrumental contribution to the line width is typically 50 arcsec while the line broadening due to thermal motion of the ions at the lowest ion temperatures of interest, say 2 keV is about 80 arcsec. Thus, ion temperatures have been deduced from line profile analysis of the resonance lines of e.g., Ar XVIII and Cl XVII with about 10 % accuracy and compared to measurements from other ion temperature diagnostics at JET. An example of ion temperatures and angular rotation velocities deduced from these measurements is given in Fig. 15 compared with similar measurements from the curved crystal spectrometer at JET[22].

D. Monochromatic mode

The fourth operational mode of the double-crystal monochromator is the determination of the time behaviour of the intensity at a fixed wavelength throughout the discharge. Since some crystals (like KAP and TlAP) show relatively intense higher order reflectivity it is possible in some cases to observe lines of two different elements in different reflection order simultaneously, simply by different discriminator setting. For instance the simultaneous oxygen and chlorine recording by observation of the lines of oxygen Lyman α (O VIII 1s - 2p at 1.8967 nm) in first order and helium-like chlorine (Cl XVI $1s^2 - 1s3p$ at 0.3794 nm) in fifth order.

The monochromatic time behaviour measurements are especially interesting to observe rapidly changing line intensities caused by fast plasma processes, such as internal instabilities or following injection of elements into the plasma by laser ablation. Fig. 16 gives examples of the time behaviour of the helium-like lines ($1s^2\ ^1S_o - 1s2p\ ^1P_1$) of Fe (above) and of Co (below) from laser ablated Fe and Co, respectively. These metal impurities were injected into plasmas which had quite different properties. While the Fe was introduced into a plasma of low particle confinement such that the line intensity decayed in about 0.3 s, the cobalt was injected into the plasma after the start of the good confinement (H-mode). The observed time behaviour together with that from lower ionization stages suggests the plasma behaved as a slightly "leaky" integrator of impurities with a confinement time of about 4 s (which is much higher than the energy confinement time), as was found from transport modelling calculations[23]. Hence the

measurements of the time behaviour of spectral line intensities at fixed wavelengths can give important information on the plasma particle confinement.

III. CONCLUSIONS

A double-crystal monochromator system with excellent shielding against neutrons and γ-rays for active-phase soft X-ray spectroscopy was built and brought into operation at JET. The first results demonstrate that the high mechanical accuracy necessary for fast spectral scans and precise wavelength measurements was achieved. They also show that the sensitivity of the instrument is good enough to obtain interesting new results for four different operational modes of the monochromator, the broad-band spectral scan, the repetitive spectral scan of characteristic groups of lines, the line scan, and the monochromatic time behaviour of spectral lines. The first measurements gave information on the impurity composition, the time behaviour during the discharge, the impurity confinement and the processes populating excited atomic levels. With the absolute calibration of the instrument performed using a specially developed large-area X-ray source absolute line intensity measurements are now possible.

Acknowledgements

The authors are grateful to Drs. C. Andelfinger, W. Engelhardt and H. Röhr for their continuous support throughout the course of the project and to Drs. K. Behringer, R. Giannella, N.C. Hawkes, H. Krause, F. Mompéan, H.P. Summers, P. Thomas and R. Willingale for many fruitful discussions and help. Thanks go to P. Abel, J. Fink, H.E. Clarke, R. Lobel, H. Maier, T. Patel, G. Riemenschneider, J. Ryan, H. Schäfer, H.-B. Schilling, G. Schmitt, G. Snelling and B. Viaccoz for continuous support during construction and commissioning of the device, as well as to the JET team for operating the tokamak.

References

[1] M. Bitter, S. von Goeler, R. Horton, M. Goldman, K.W. Hill, N.R. Sauthoff, and W. Stodiek, Phys, Rev. Lett. **42**, 304 (1979)

[2] C. de Michelis and M. Mattioli, Nucl. Fusion **21**, 677 (1981)

[3] E. Källne and J. Källne, Phys. Scr. **T17**, 152 (1987)

[4] R. Barnsley, K.D. Evans, N.J. Peacock, and N.C. Hawkes, Rev. Sci. Instrum. **57**, 2159 (1986)

[5] W. Engelhardt, J. Fink, G. Fussmann, H. Krause, H.-B. Schilling, and U. Schumacher, MPI für Plasmaphysik, Garching, Report IPP1/212, IPP III/81, 1982

[6] C. Andelfinger, J. Fink, G. Fussmann, H. Krause, H. Röhr, H.-B. Schilling, U. Schumacher, P. Becker, H. Siegert, P. Abel, J. Keul, MPI für Plasmaphysik, Garching, Report IPP 1/225, 1984
J. Keul, P. Abel, Proc. 12th Symp. on Fusion Engineering, Monterey, CA, 1512 (1987)

[7] G. Rupprecht, JET-Report JET-R(88) 13, 1988

[8] U. Schumacher, E. Källne, H.W. Morsi, and G. Rupprecht, Rev. Sci. Instrum. **60**, 562 (1989)

[9] U. Schumacher, Nucl. Instrum. Methods A**251**, 564 (1986) and Nucl. Instrum. Methods A**259**, 538 (1987)

[10] M. Lewis, Ph.D. Thesis, University of Leicester, 1982

[11] J. Fink, H.W. Morsi, H. Röhr, and U. Schumacher, MPI für Plasmaphysik Report IPP 1/240 (1987)

[12] W. Bier, K. Schubert, H. Röhr, and U. Schumacher, Rev. Sci. Instrum. **60**, 567 (1989)

[13] H.W. Morsi, H. Röhr, and U. Schumacher, Z. Naturforsch. **42A**, 1051 (1987)

[14] J.S. Thomson, in "X-Ray Spectroscopy" (ed. L.V. Azaroff), chapter 2, McGraw-Hill Book Company, New York, 1974

[15] TFR Group, M. Cornille, J. Dubau, M. Loulergue, Phys. Rev. A**32**, 3000 (1985)

[16] F. Bombarda, R. Giannella, E. Källne, G.J. Tallents, F. Bely-Dubau, P. Faucher, M. Cornille, J. Dubau, and A.H. Gabriel, Phys. Rev. A**37**, 504 (1988)

[17] M. Bitter, H. Hsuan, J.E. Rice, K.W. Hill, M. Diesso, B. Grek, R. Hulse, D.W. Johnson, L.C. Johnson, and S. von Goeler, Rev. Sci. Instrum. **59**, 2131 (1988)

[18] F.P. Keenan, S.M. McCann, R. Barnsley, J. Dunn, K.D. Evans, and N.J. Peacock, Phys. Rev. A**39**, 4092 (1989)

[19] Calculations by H.P. Summers and K. Behringer, private communication

[20] J.E. Rice, E.S. Marmar, J.L. Terry, E. Källne, J. Källne, Phys. Rev. Lett. **56**, 50 (1986) and
M. Mattioli, N.J. Peacock, H.P. Summers, B. Denne, N.C. Hawkes, JET-Report JET-P(89)06, and Phys. Rev. A**40**, 3886 (1989)

[21] R. Barnsley, U. Schumacher, E. Källne, H.W. Morsi, and G. Rupprecht, Proc. 16th Europ. Conf. on Controlled Fusion and Plasma Physics, Venice, Vol. **13B**, Part IV, 1557 (1989)

[22] A. Stenflo, MSC Thesis, Department of Physics I, Royal Institute of Technology, Stockholm 1990

[23] N.C. Hawkes, Z. Wang, R. Barnsley, K. Behringer, S. Cohen, B. Denne, A. Edwards, R. Giannella, R. Gill, G. Magyar, D. Pasini, N. Peacock, U. Schumacher, C. Vieider, D. Zasche, Proc. 16th Europ. Conf. on Controlled Fusion and Plasma Physics, Venice, Vol. **13B**, Part I, 79 (1989)

Figure captions

Fig. 1 Scheme of the radiation-shielded double-crystal X-ray monochromator

Fig. 2 Lay-out of the double-crystal monochromator and the beam line to the JET torus

Fig. 3 Accessible spectral ranges in photon energy ε (upper scale) or in wavelength λ (lower scale) covered by the active phase double-crystal monochromator for different crystal lattice spacings 2d.

Fig. 4 Double-crystal rocking curves of Topaz(303) measured using the double-crystal monochromator for the $K\alpha_1$ lines of Ni, Fe and Cr.

Fig. 5 Double-crystal rocking curve of TlAP at $NiL\alpha_{1,2}$

Fig. 6 The $CrK\alpha$ spectrum measured with Topaz(303) crystals using the fine (high resolution) collimator

Fig. 7 Example of the angle difference of both crystals in the monochromator recorded for a wavelength scan during a JET discharge. There are two traces for each crystal (b and c resp. d and e) showing the encoder readings for every 20 ms; b and c are the encoders for both rotational directions of crystal 1, and d and e are those for the second crystal. The top trace (a) shows the resulting parallelism error deduced from the encoder readings. The bottom trace (f) shows the measured line intensity for each scan during the discharge (12 scans in 6 seconds).

Fig. 8 Calibration factor for the double-crystal monochromator versus wavelength for Topaz(303) crystals, the large error bars reflect the cumulative effects of the calibration source error, the uncertainties in the solid angle relation estimates and others.

Fig. 9 Broad band spectrum obtained using TlAP crystals covering the wavelength range from 1.13 nm to 1.95 nm with Ne-like Ni lines and the Lyman series of oxygen during a time interval of relatively constant plasma parameters

Fig. 10 Repetitive scan of a narrow wavelength region reflecting the time behaviour of Ni XXVII

Fig. 11 He-like spectra of Cl, Cr and Ni

Fig. 12 Repetitive scan of the oxygen Lyman series versus time

Fig. 13 Oxygen Lyman line intensities versus quantum number n normalized to the calculated values[19]

Fig. 14 Line scans for neon-like nickel (above) and oxygen Lyman α (below) throughout two consecutive discharges at JET

Fig. 15 Temporal behaviour of ion temperature (a) and angular rotation velocity (b) obtained from the double-crystal monochromator (solid points) compared to similar results from the curved crystal spectrometer (solid line). (c) indicates the neutral beam power.

Fig. 16 Time behaviour of He-like Fe (above) and Co (below) line intensities during a JET discharge with laser ablation of Fe at 11 s and Co at 13 s, respectively.

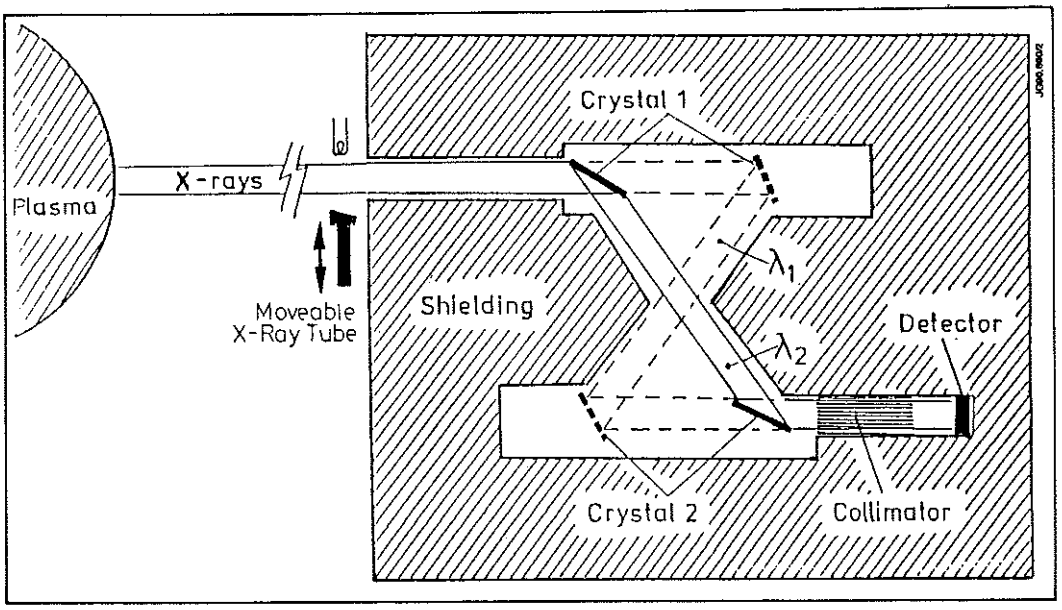

Fig. 1 Scheme of the radiation-shielded double-crystal X-ray monochromator

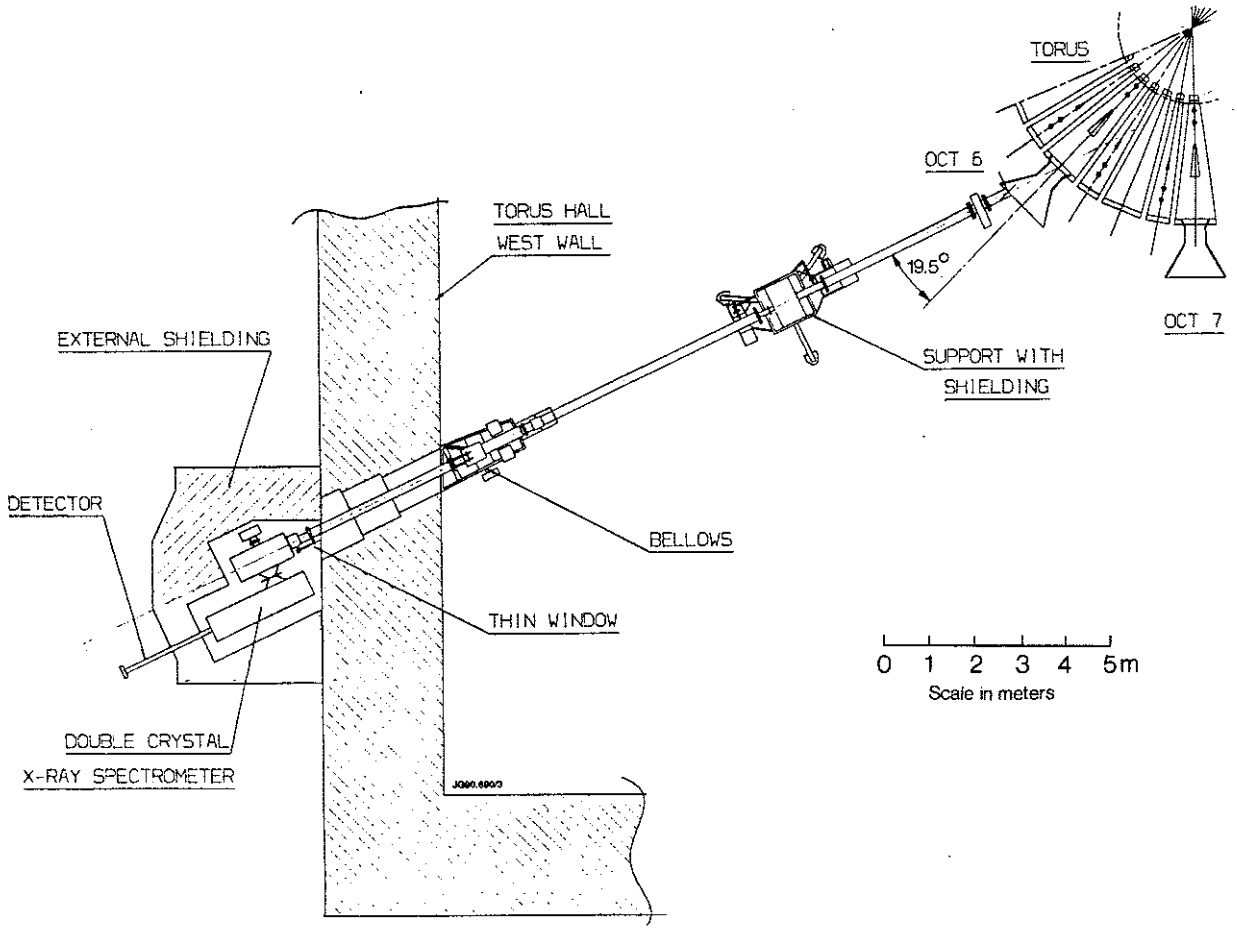

Fig. 2 Lay-out of the double-crystal monochromator and the beam line to the JET torus

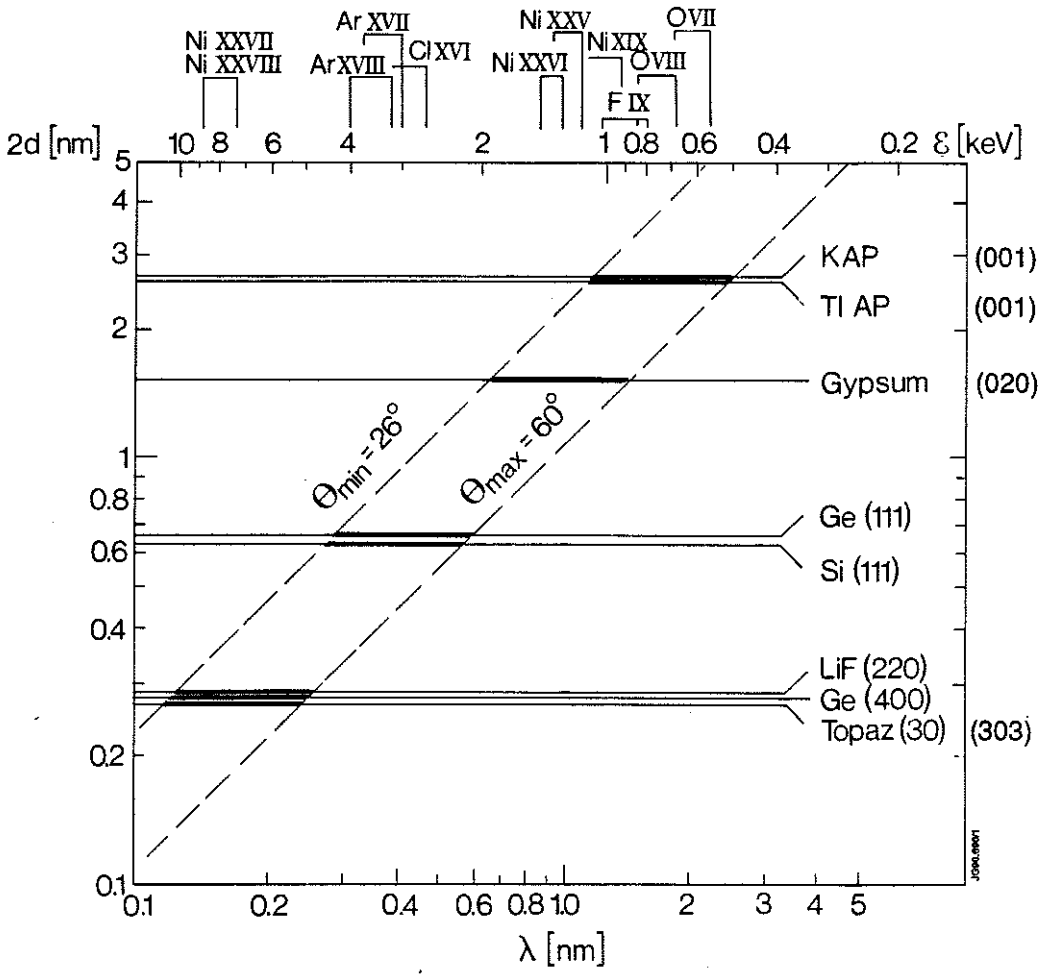

Fig. 3 Accessible spectral ranges in photon energy ε (upper scale) or in wavelength λ (lower scale) covered by the active phase double-crystal monochromator for different crystal lattice spacings 2d.

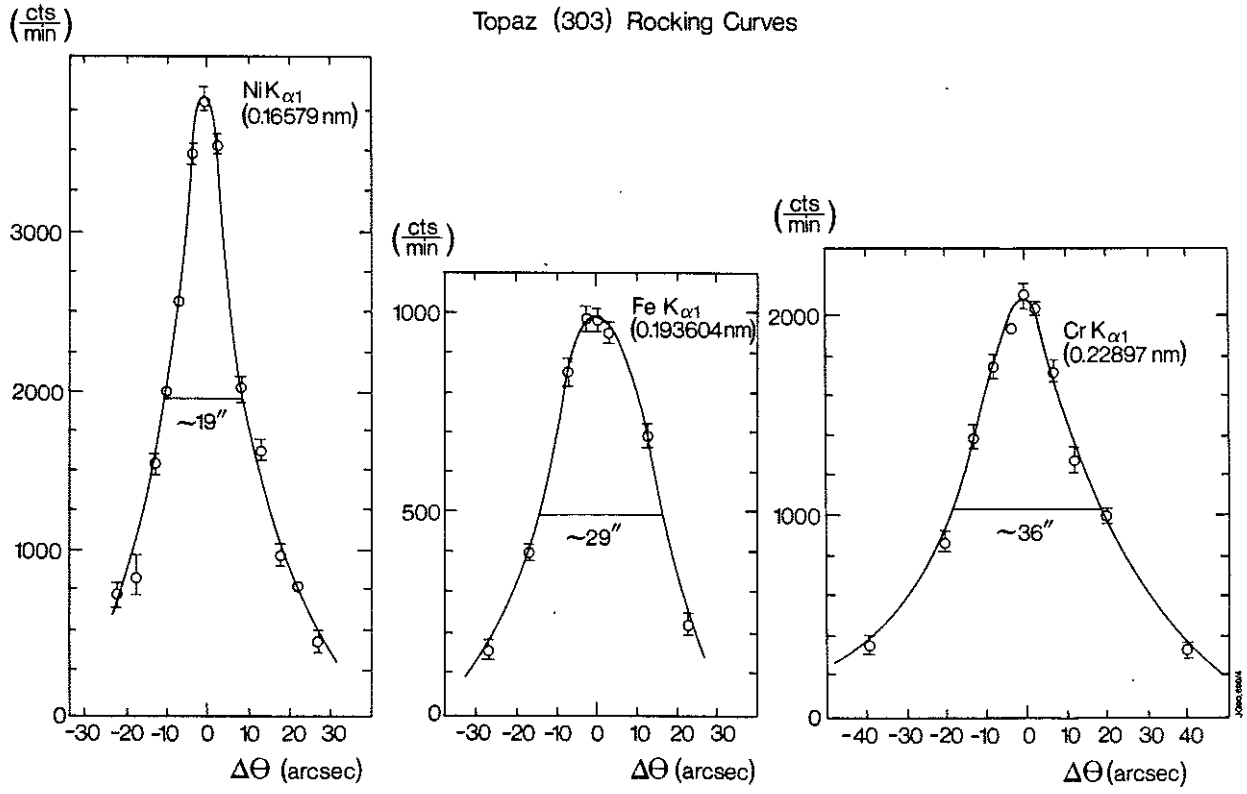

Fig. 4 Double-crystal rocking curves of Topaz(303) measured using the double-crystal monochromator for the $K\alpha_1$ lines of Ni, Fe and Cr.

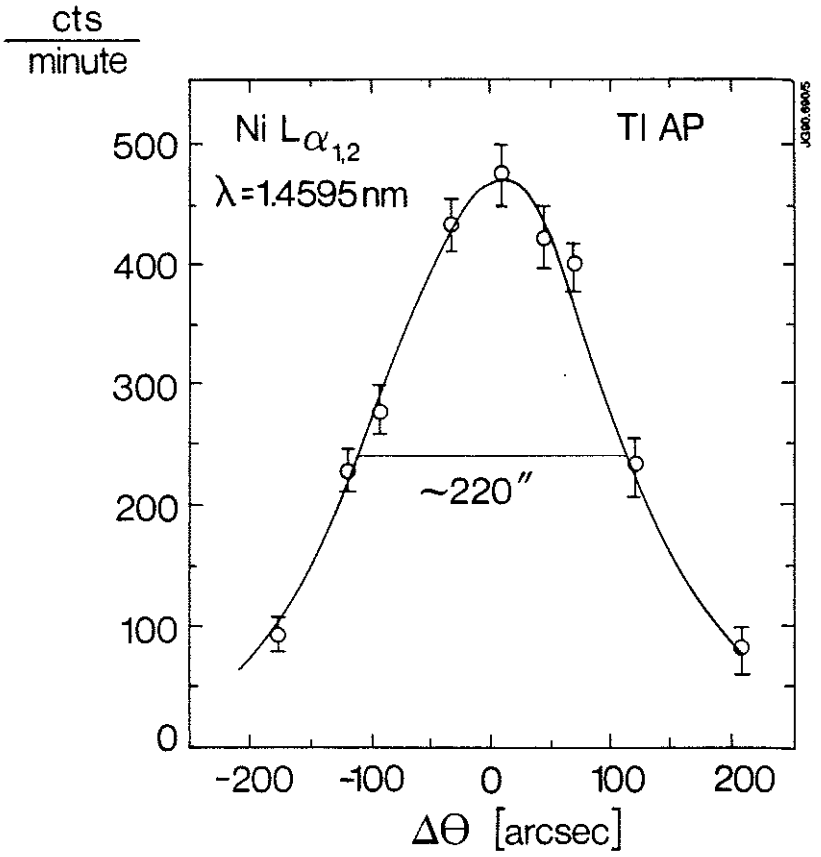

Fig. 5 Double-crystal rocking curve of TlAP at NiL$\alpha_{1,2}$

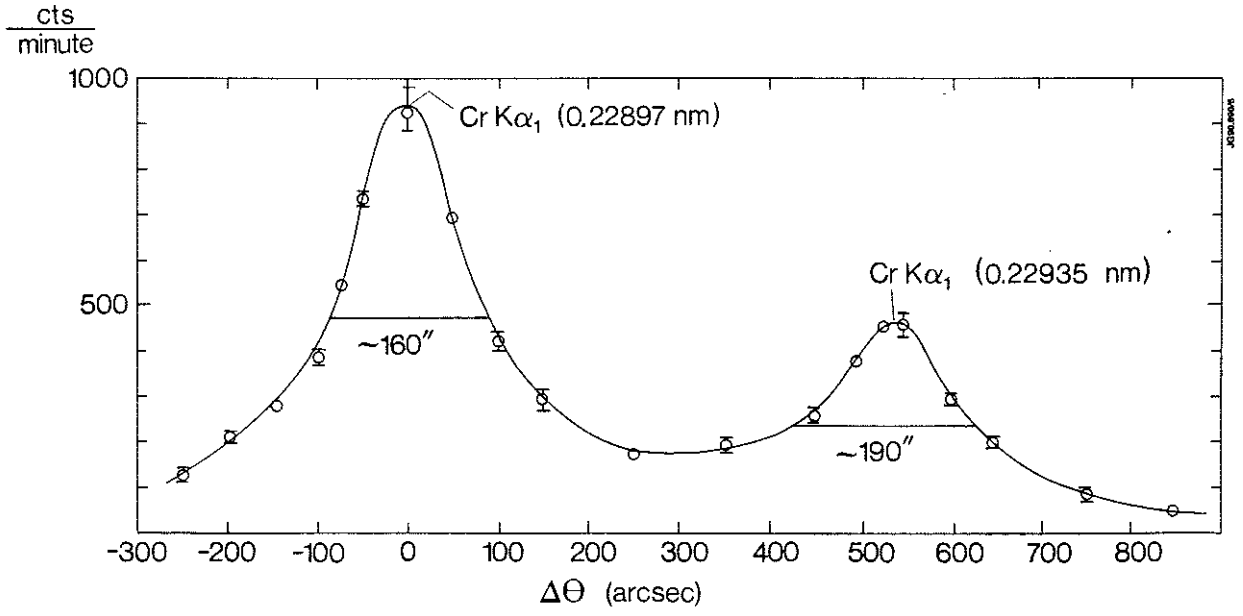

Fig. 6 The CrKα spectrum measured with Topaz(303) crystals using the fine (high resolution) collimator

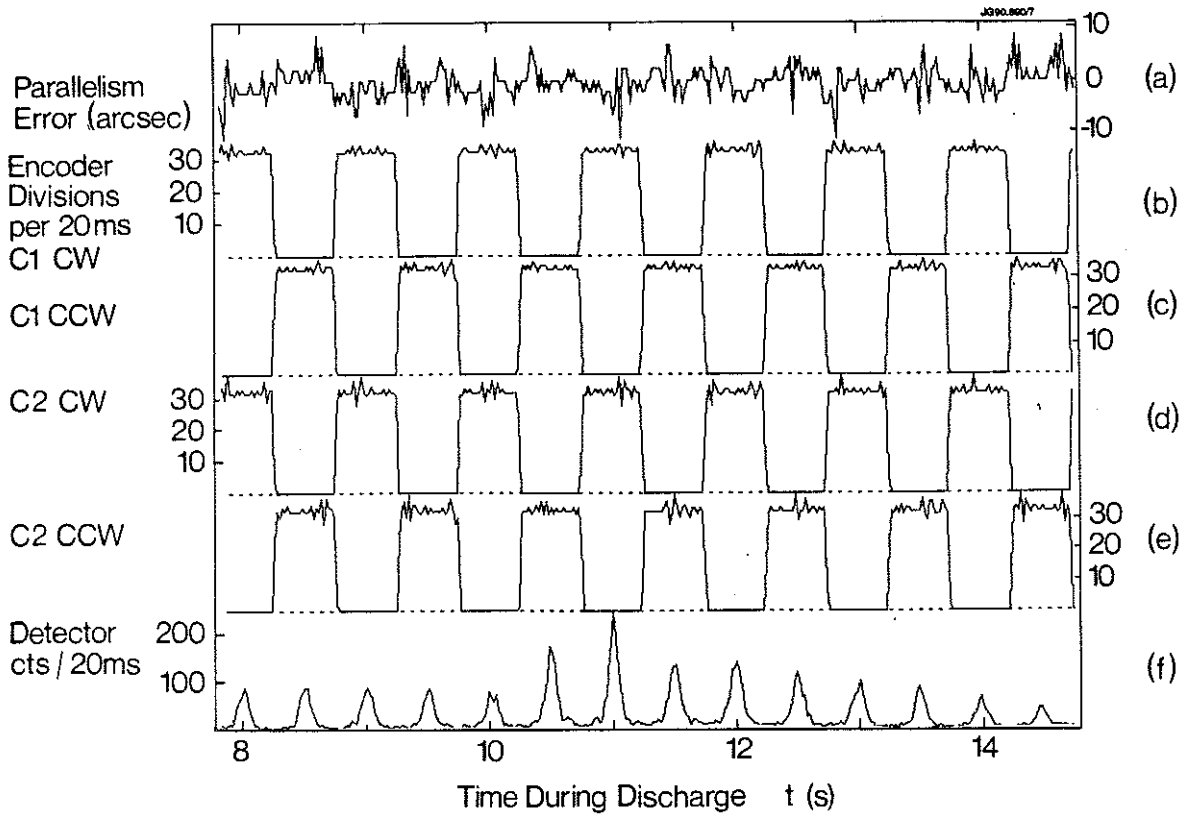

Fig. 7 Example of the angle difference of both crystals in the monochromator recorded for a wavelength scan during a JET discharge

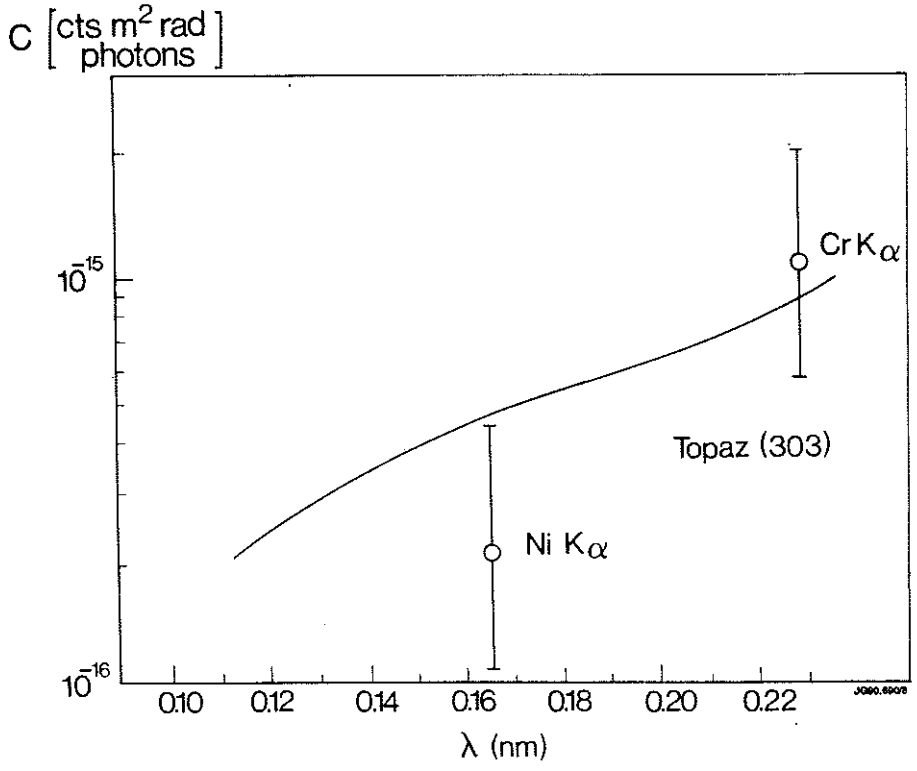

Fig. 8 Calibration factor for the double-crystal monochromator versus wavelength for Topaz(303) crystals

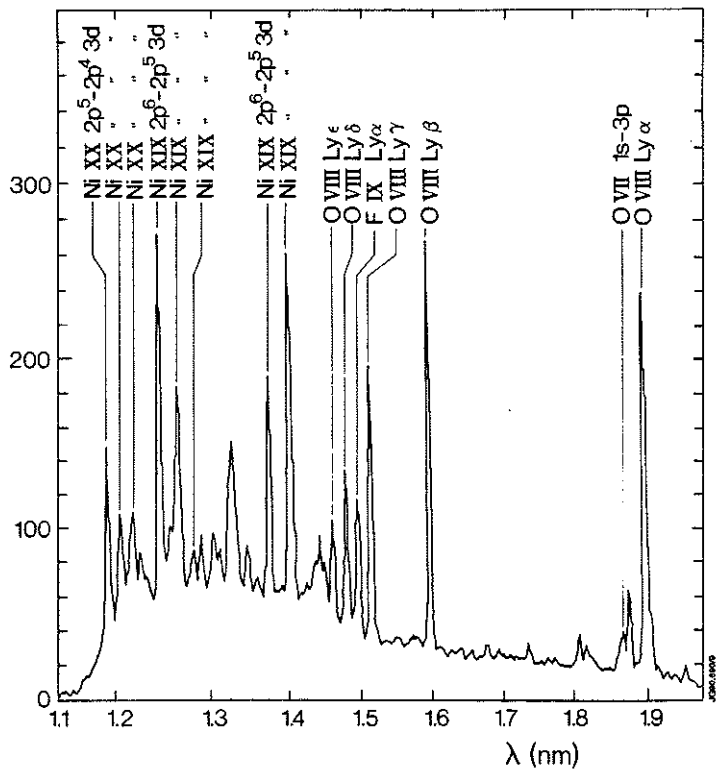

Fig. 9 Broad band spectrum obtained using TlAP crystals covering the wavelength range from 1.13 nm to 1.95 nm with Ne-like Ni lines and the Lyman series of oxygen during a time interval of relatively constant plasma parameters

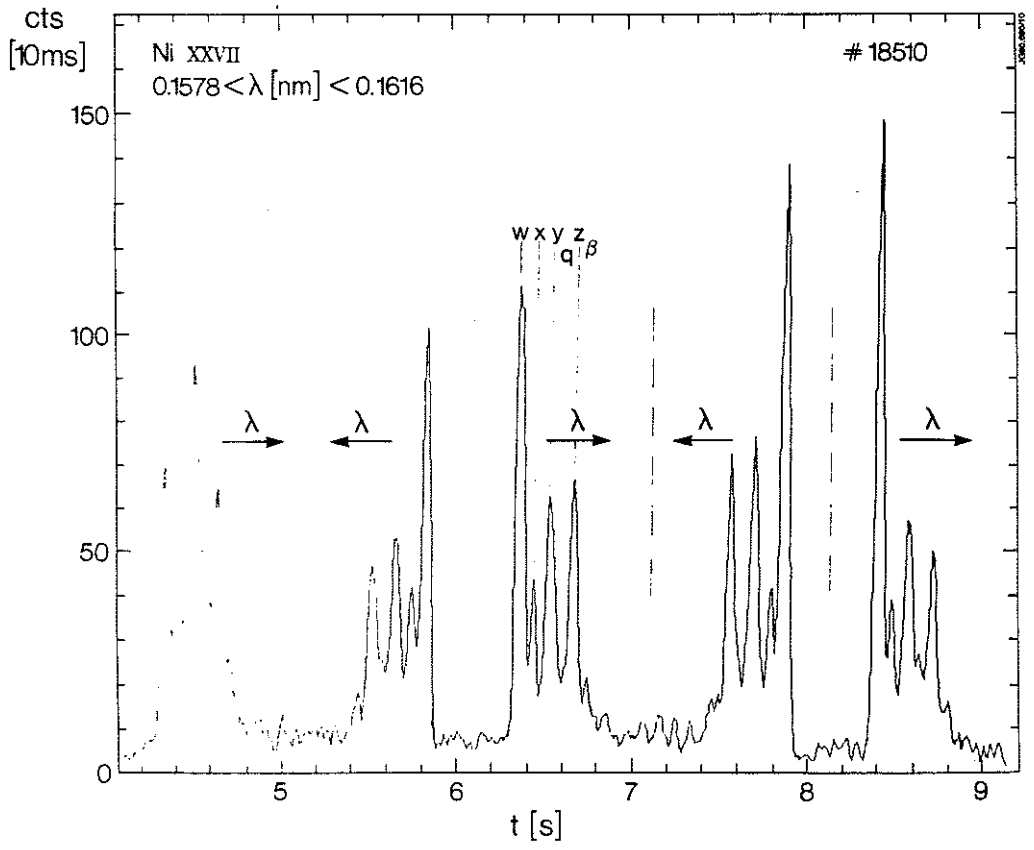

Fig. 10 Repetitive scan of a narrow wavelength region reflecting the time behaviour of Ni XXVII

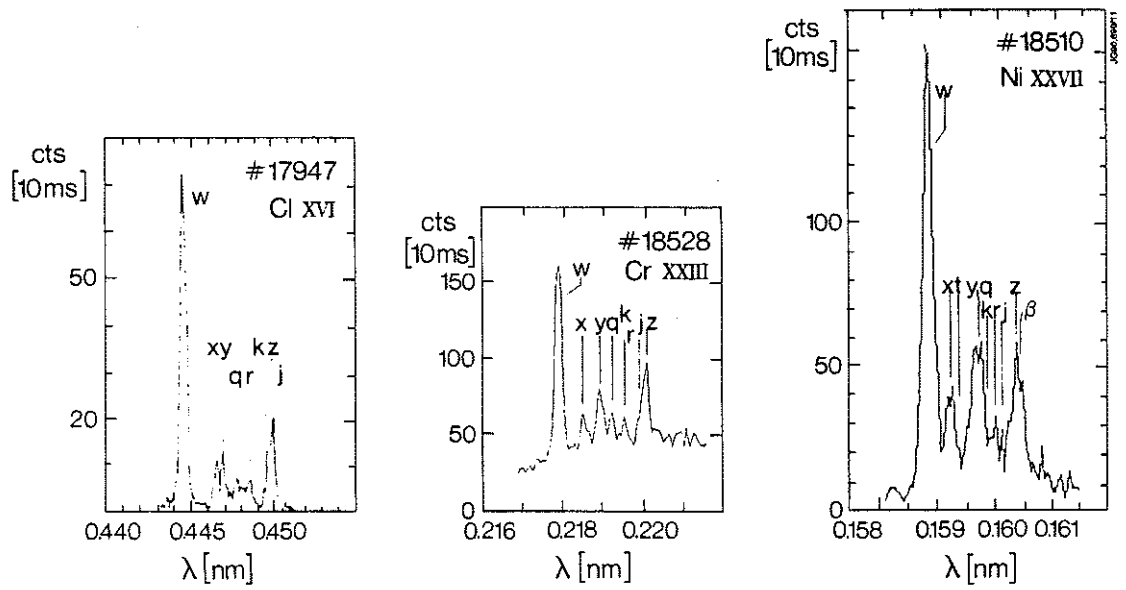

Fig. 11 He-like spectra of Cl, Cr and Ni

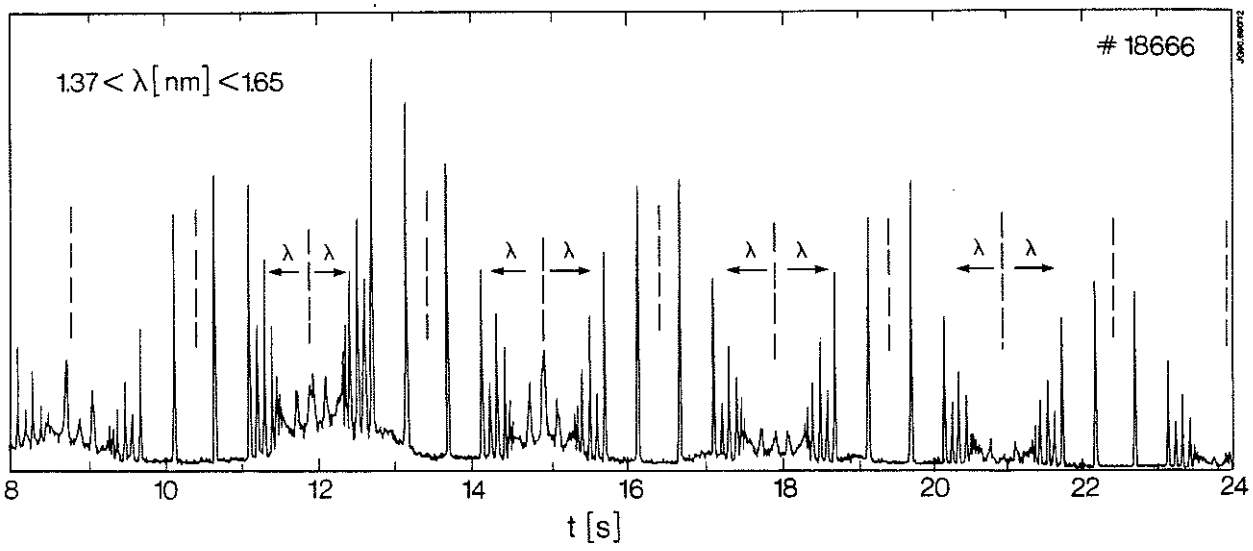

Fig. 12 Repetitive scan of the oxygen Lyman series versus time

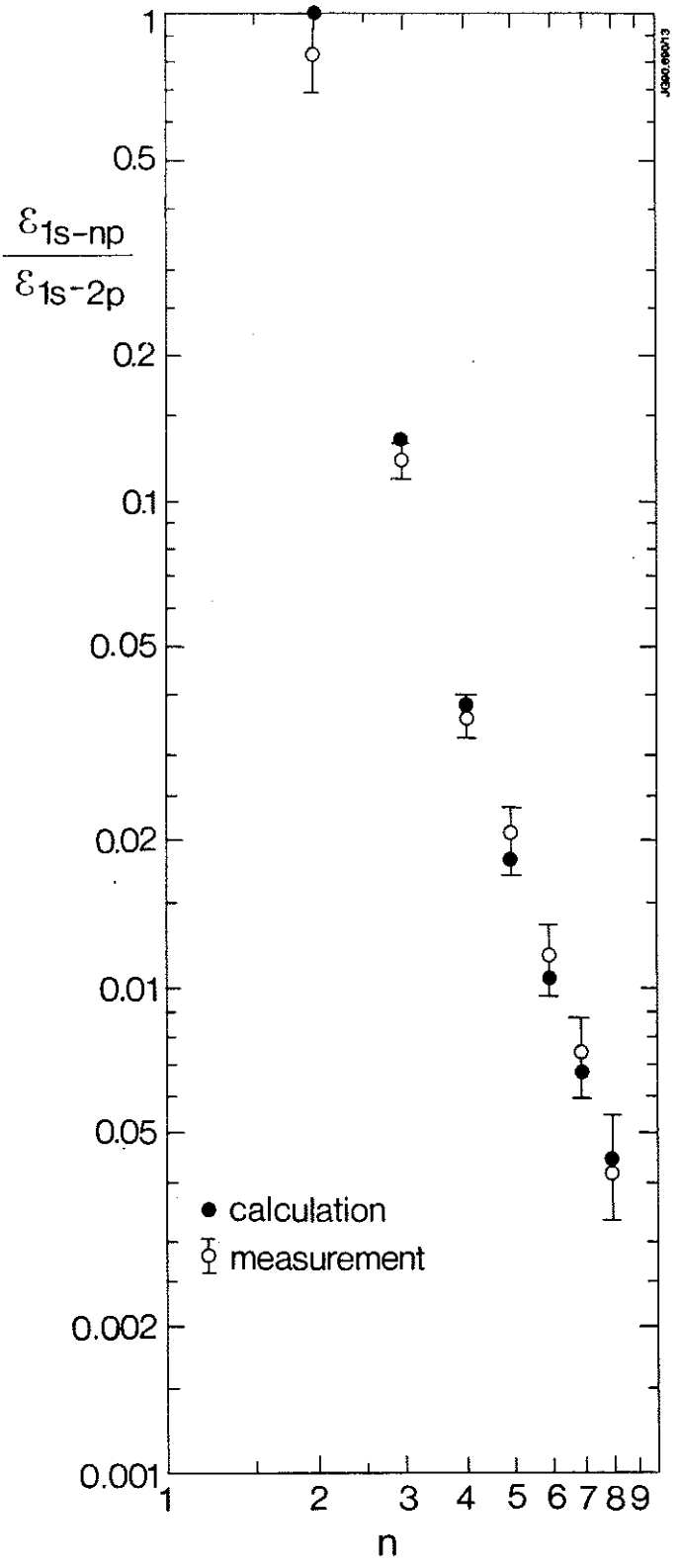

Fig. 13 Oxygen Lyman line intensities versus quantum number n normalized to the calculated values[18]

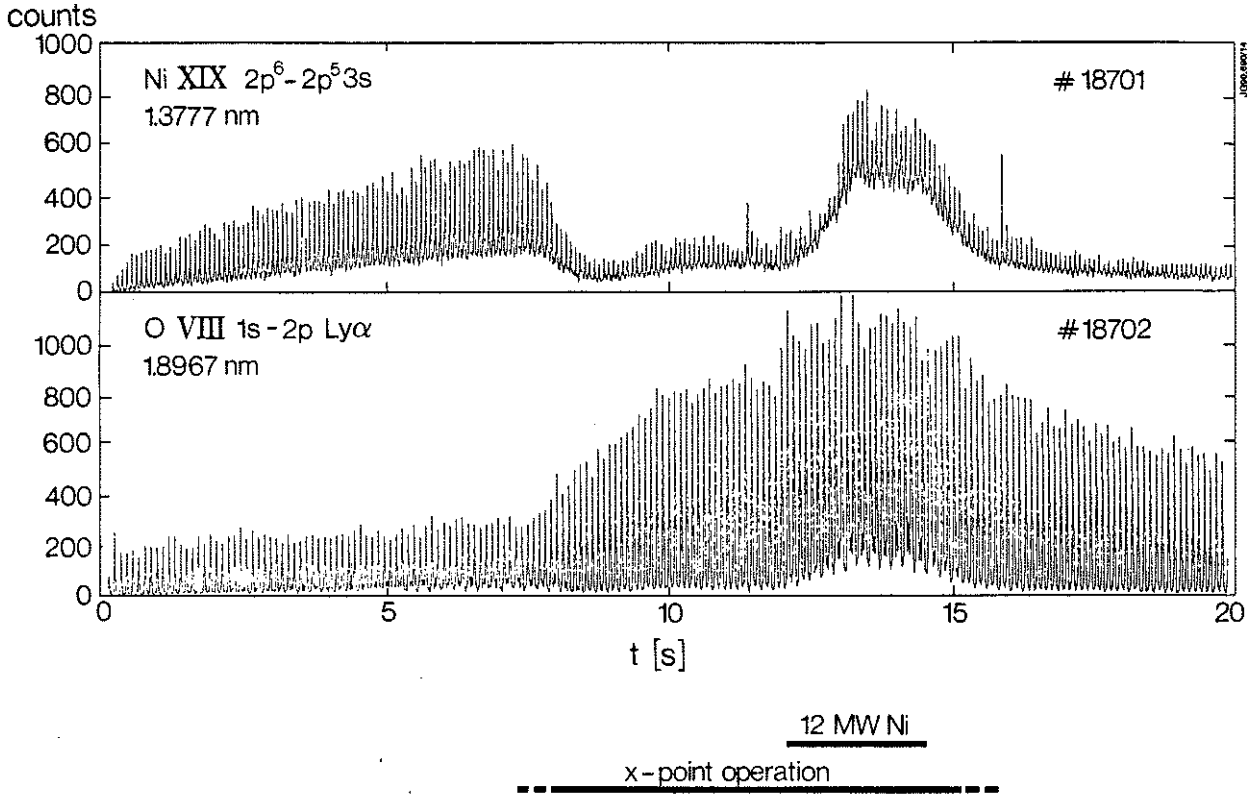

Fig. 14 Line scans for neon-like nickel (above) and oxygen Lyman α (below) throughout two consecutive discharges at JET

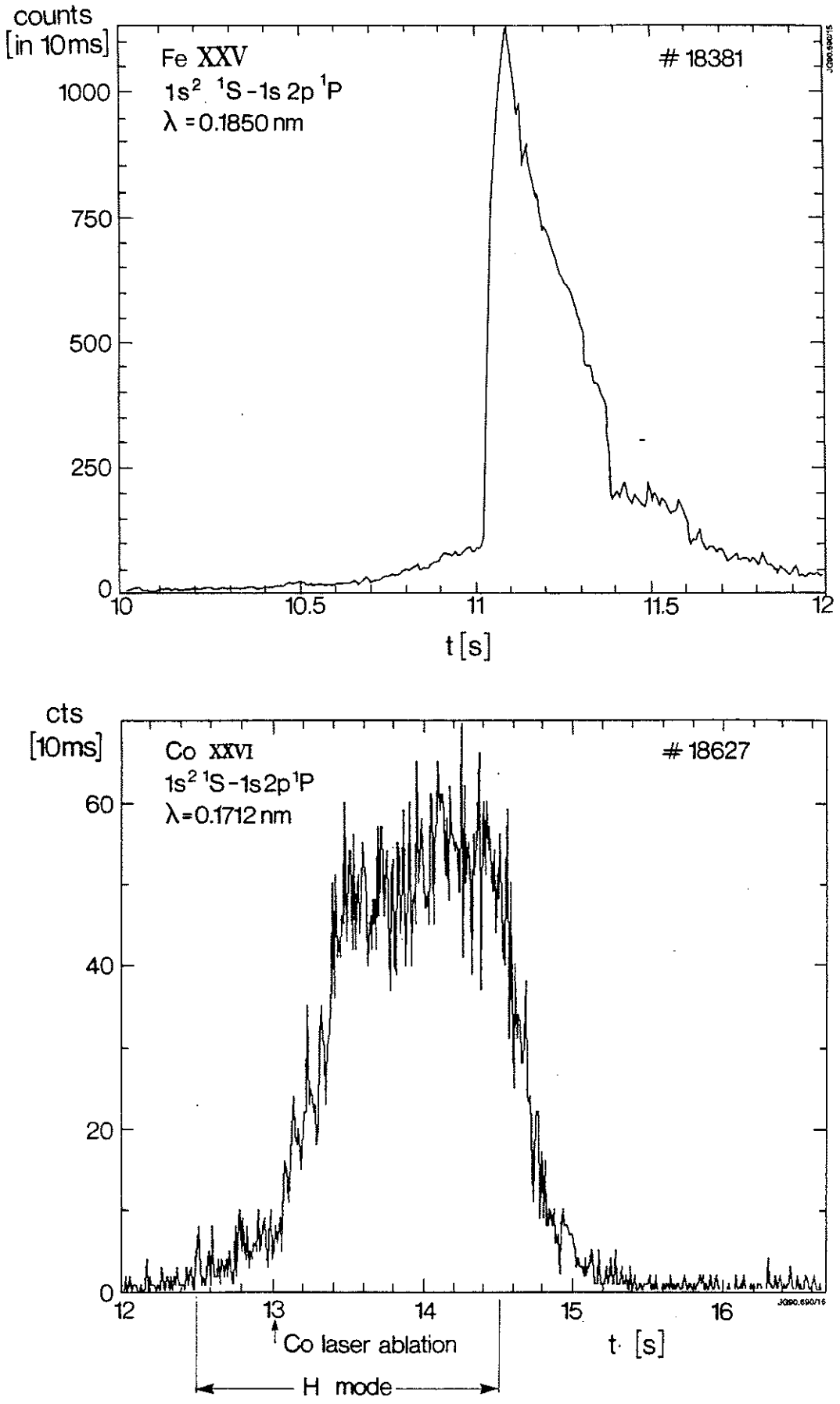

Fig. 15 Time behaviour of He-like Fe (above) and Co (below) line intensities during a JET discharge with laser ablation of Fe at 11 s and Co at 13 s, respectively.

APPENDIX 1.

THE JET TEAM

JET Joint Undertaking, Abingdon, Oxon, OX14 3EA, U.K.

J.M.Adams[1], F.Alladio[4], H.Altmann, R.J.Anderson, G.Appruzzese, W.Bailey, B.Balet, D.V.Bartlett, L.R.Baylor[24], K.Behringer, A.C.Bell, P.Bertoldi, E.Bertolini, V.Bhatnagar, R.J.Bickerton, A.Boileau[3], T.Bonicelli, S.J.Booth, G.Bosia, M.Botman, D.Boyd[31], H.Brelen, H.Brinkschulte, M.Brusati, T.Budd, M.Bures, T.Businaro[4], H.Buttgereit, D.Cacaut, C.Caldwell-Nichols, D.J.Campbell, P.Card, J.Carwardine, G.Celentano, P.Chabert[27], C.D.Challis, A.Cheetham, J.Christiansen, C.Christodoulopoulos, P.Chuilon, R.Claesen, S.Clement[30], J.P.Coad, P.Colestock[6], S.Conroy[13], M.Cooke, S.Cooper, J.G.Cordey, W.Core, S.Corti, A.E.Costley, G.Cottrell, M.Cox[7], P.Cripwell[13], F.Crisanti[4], D.Cross, H.de Blank[16], J.de Haas[16], L.de Kock, E.Deksnis, G.B.Denne, G.Deschamps, G.Devillars, K.J.Dietz, J.Dobbing, S.E.Dorling, P.G.Doyle, D.F.Düchs, H.Duquenoy, A.Edwards, J.Ehrenberg[14], T.Elevant[12], W.Engelhardt, S.K.Erents[7], L.G.Eriksonn[5], M.Evrard[2], H.Falter, D.Flory, M.Forrest[7], C.Froger, K.Fullard, M.Gadeberg[11], A.Galetsas, R.Galvao[8], A.Gibson, R.D.Gill, A.Gondhalekar, C.Gordon, G.Gorini, C.Gormezano, N.A.Gottardi, C.Gowers, B.J.Green, F.S.Griph, M.Gryzinski[26], R.Haange, G.Hammett[6], W.Han[9], C.J.Hancock, P.J.Harbour, N.C.Hawkes[7], P.Haynes[7], T.Hellsten, J.L.Hemmerich, R.Hemsworth, R.F.Herzog, K.Hirsch[14], J.Hoekzema, W.A.Houlberg[24], J.How, M.Huart, A.Hubbard, T.P.Hughes[32], M.Hugon, M.Huguet, J.Jacquinot, O.N.Jarvis, T.C.Jernigan[24], E.Joffrin, E.M.Jones, L.P.D.F.Jones, T.T.C.Jones, J.Källne, A.Kaye, B.E.Keen, M.Keilhacker, G.J.Kelly, A.Khare[15], S.Knowlton, A.Konstantellos, M.Kovanen[21], P.Kupschus, P.Lallia, J.R.Last, L.Lauro-Taroni, M.Laux[33], K.Lawson[7], E.Lazzaro, M.Lennholm, X.Litaudon, P.Lomas, M.Lorentz-Gottardi[2], C.Lowry, G.Magyar, D.Maisonnier, M.Malacarne, V.Marchese, P.Massmann, L.McCarthy[28], G.McCracken[7], P.Mendonca, P.Meriguet, P.Micozzi[4], S.F.Mills, P.Millward, S.L.Milora[24], A.Moissonnier, P.L.Mondino, D.Moreau[17], P.Morgan, H.Morsi[14], G.Murphy, M.F.Nave, M.Newman, L.Nickesson, P.Nielsen, P.Noll, W.Obert, D.O'Brien, J.O'Rourke, M.G.Pacco-Düchs, M.Pain, S.Papastergiou, D.Pasini[20], M.Paume[27], N.Peacock[7], D.Pearson[13], F.Pegoraro, M.Pick, S.Pitcher[7], J.Plancoulaine, J-P.Poffé, F.Porcelli, R.Prentice, T.Raimondi, J.Ramette[17], J.M.Rax[27], C.Raymond, P-H.Rebut, J.Removille, F.Rimini, D.Robinson[7], A.Rolfe, R.T.Ross, L.Rossi, G.Rupprecht[14], R.Rushton, P.Rutter, H.C.Sack, G.Sadler, N.Salmon[13], H.Salzmann[14], A.Santagiustina, D.Schissel[25], P.H.Schild, M.Schmid, G.Schmidt[6], R.L.Shaw, A.Sibley, R.Simonini, J.Sips[16], P.Smeulders, J.Snipes, S.Sommers, L.Sonnerup, K.Sonnenberg, M.Stamp, P.Stangeby[19], D.Start, C.A.Steed, D.Stork, P.E.Stott, T.E.Stringer, D.Stubberfield, T.Sugie[18], D.Summers, H.Summers[20], J.Taboda-Duarte[22], J.Tagle[30], H.Tamnen, A.Tanga, A.Taroni, C.Tebaldi[23], A.Tesini, P.R.Thomas, E.Thompson, K.Thomsen[11], P.Trevalion, M.Tschudin, B.Tubbing, K.Uchino[29], E.Usselmann, H.van der Beken, M.von Hellermann, T.Wade, C.Walker, B.A.Wallander, M.Walravens, K.Walter, D.Ward, M.L.Watkins, J.Wesson, D.H.Wheeler, J.Wilks, U.Willen[12], D.Wilson, T.Winkel, C.Woodward, M.Wykes, I.D.Young, L.Zannelli, M.Zarnstorff[6], D.Zasche[14], J.W.Zwart.

PERMANENT ADDRESS

1. UKAEA, Harwell, Oxon. UK.
2. EUR-EB Association, LPP-ERM/KMS, B-1040 Brussels, Belgium.
3. Institute National des Récherches Scientifique, Quebec, Canada.
4. ENEA-CENTRO Di Frascati, I-00044 Frascati, Roma, Italy.
5. Chalmers University of Technology, Göteborg, Sweden.
6. Princeton Plasma Physics Laboratory, New Jersey, USA.
7. UKAEA Culham Laboratory, Abingdon, Oxon. UK.
8. Plasma Physics Laboratory, Space Research Institute, Sao José dos Campos, Brazil.
9. Institute of Mathematics, University of Oxford, UK.
10. CRPP/EPFL, 21 Avenue des Bains, CH-1007 Lausanne, Switzerland.
11. Risø National Laboratory, DK-4000 Roskilde, Denmark.
12. Swedish Energy Research Commission, S-10072 Stockholm, Sweden.
13. Imperial College of Science and Technology, University of London, UK.
14. Max Planck Institut für Plasmaphysik, D-8046 Garching bei München, FRG.
15. Institute for Plasma Research, Gandhinagar Bhat Gujat, India.
16. FOM Instituut voor Plasmafysica, 3430 Be Nieuwegein, The Netherlands.
17. Commissiariat à L'Energie Atomique, F-92260 Fontenay-aux-Roses, France.
18. JAERI, Tokai Research Establishment, Tokai-Mura, Naka-Gun, Japan.
19. Institute for Aerospace Studies, University of Toronto, Downsview, Ontario, Canada.
20. University of Strathclyde, Glasgow, G4 ONG, U.K.
21. Nuclear Engineering Laboratory, Lapeenranta University, Finland.
22. JNICT, Lisboa, Portugal.
23. Department of Mathematics, Univeristy of Bologna, Italy.
24. Oak Ridge National Laboratory, Oak Ridge, Tenn., USA.
25. G.A. Technologies, San Diego, California, USA.
26. Institute for Nuclear Studies, Swierk, Poland.
27. Commissiariat à l'Energie Atomique, Cadarache, France.
28. School of Physical Sciences, Flinders University of South Australia, South Australia SO42.
29. Kyushi University, Kasagu Fukuoka, Japan.
30. Centro de Investigaciones Energeticas Medioambientales y Techalogicas, Spain.
31. University of Maryland, College Park, Maryland, USA.
32. University of Essex, Colchester, UK.
33. Akademie de Wissenschaften, Berlin, DDR.

CR 88.49.1A